Intermediate Wetting State at Nano/Microstructured Surfaces

Gyoko NAGAYAMA*, Dejian ZHANG

A general partial wetting model to describe an intermediate wetting state is proposed in this study to explain the deviations between the experimental results and classical theoretical wetting models for hydrophobic surface. We derived the theoretical partial wetting model for the static intermediate wetting state based on the thermodynamic energy minimization method. The contact angle based on the partial wetting model is a function of structural parameters and effective wetting ratio *f*, which agrees with the classical Wenzel and Cassie–Baxter models at *f*=1 and 0, respectively. Si samples including porous surfaces, patterned surfaces and hierarchical nano/microstructured surfaces were prepared experimentally, having same chemical composition but different physical morphology. We found that the experimental water contact angles deviate significantly from the classical Wenzel and Cassie–Baxter models but show good agreement with the proposed partial wetting model.

1. Introduction

Nature-inspired artificial surfaces[1–5] with controllable wettability attract much interest in various engineering and industrial technologies, such as high-performance nano/microscale thermal fluidic systems, bio-chips for DNA detection, and membrane electrode assemblies for micro fuel cell systems.[6–12] Basically, wettability can be controlled by varying physical morphology and chemical composition to fabricate hydrophobic, superhydrophobic, hydrophilic, and superhydrophilic surfaces.[13–18] Regarding the effect of physical morphology on wettability, Wenzel model represents the fully-wetted state, while Cassie–Baxter model describes the non-wetted state on rough surfaces.[19,20] However, a perfect state of Wenzel or Cassie–Baxter model is rare in real situations.[21] An intermediate state, i.e., the mixed-wetting state or the partial wetting state, exists between the Wenzel and Cassie–Baxter states.[22–27] Effective wetting ratio *f* has been initially introduced as a dominant factor for the partial wetting model, which represents the proportion of liquid wetting into the structure. It is clear that *f* ranges from *f*=0 at the non-wetted Cassie–Baxter state to *f*=1 at the fully wetted Wenzel state (see Fig. 1).[28] To obtain a clear understanding of wetting behavior on the structured surface, the classical Wenzel and Cassie−Baxter models are insufficient and further studies on the intermediate state are necessary.

To date, wetting is commonly described by the contact angle or contact angle hysteresis, placing less emphasis on the detailed wetting state or effective wetting area (i.e. real contact area) in the vicinity of the solid–liquid–vapor interface. A significant number of studies have been conducted on the dynamic wetting transition from Cassie–Baxter state to Wenzel state.[29–31] The process is a forced dynamic wetting transition accompanying with a time dependent contact angle. It occurs under external stimuli, showing a dependence on the degree of the driving force (to provide activation energy to overcome the transition barrier). That is, the wetting transition will not occur spontaneously and a time-independent wetting state will be kept for a droplet under equilibrium condition.[30,32,33] Therefore, the static contact angle plays important role to describe the intrinsic wettability of a given solid–liquid system. On the other hand, a number of experimental static water contact angles disagree with either the theoretical Wenzel contact angles or the Cassie–Baxter ones.[26,34–38] For example, the experimental water contact angles conducted by Erbil et al. at superhydrophobic surfaces were larger than those predicted by Wenzel or Cassie–Baxter models.[37,38] Significant deviations between the experimental and the theoretical results also have been reported,[26,34–36] implying an intermediate wetting state between Wenzel and Cassie–Baxter states. Miwa et al. first proposed a mix-wetting state and Marmur discussed in more details later.[22,23] Further studies conducted by Luo et al. demonstrated the stable intermediate wetting state at the surfaces patterned by parallel microchannels and periodic micropillars.[24,25] Yang et al. discussed intermediate wetting state based on the Gibbs's interfacial free energy principle and they also observed a static intermediate wetting state on an anodic aluminum

oxide film surfaces.[26] Furthermore, a combined Cassie–Baxter/Wenzel state was reported by Liu et al. for a static droplet condensed on a lotus leaf surface.[36] These studies provided sufficient evidences on the existence of the static intermediate wetting state at the structured surfaces. However, the underlying mechanism of the static intermediate wetting state is still open for questions and a general model is necessary to describe the contact angle for the intermediate wetting state.

A general theoretical model of intermediate wetting state for the static contact angle is possible to be obtained by minimizing the surface free energy of a system consisting of a structured surface and droplet. In the past few decades, thermodynamic analysis based on the minimum energy principle of a system consisting of a solid surface and droplet, has been applied to derive the Young's model at a flat surface system[39,40] and the Wenzel/Cassie–Baxter models at structured surface systems.[23,41] Sajadinia et al. proposed a combination model of the Wenzel and Cassie–Baxter states for the dual scale structures consisting of nanopillars and micropillars.[42] Since the sidewalls at the dual scale structures were assumed to be flat in the combination model by Sajadinia et al., Wu et al. performed numerical simulations including the structured sidewalls, showing a result of significant enhancement on superhydrophobic stability.[43] These previous studies provide the methodologies on the energy minimization analysis at the nano/microstructured surfaces, while the wetting states are limited to various combinations of the full wetting (Wenzel) and the non-wetting (Cassie–Baxter) states.

In this study, we focus on the intermediate wetting state between the Wenzel and Cassie–Baxter states. A partial wetting model is proposed based on the energy minimization for the static intermediate wetting state characterized by the effective wetting ratio. Microstructured and nano/micro hierarchically structured surfaces were prepared on silicon (Si) substrates and the contact angles were measured experimentally. The effective wetting ratio at the structured surface was estimated based on the experimental data and an empirical equation as a function of surface solid fraction and fractal dimension was proposed. Furthermore, a comparison between experimental results and theoretical wetting models was drawn.

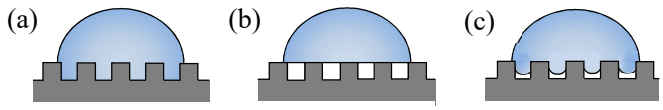

Fig. 1 Schematics of wetting states on structured surfaces for: (a) Wenzel model, (b) Cassie–Baxter model and (c) partial wetting model.

2. Methods

2.1 Theoretical Models

From the macroscopic viewpoint, surface wettability is usually evaluated by contact angle. For an equilibrium droplet at flat surface, the contact angle θ_Y predicted by Young's equation in a solid–liquid–vapor system is

$$\cos\theta_Y = \frac{\gamma_{sv} - \gamma_{sl}}{\gamma_{lv}} \quad (1)$$

where γ_{sl}, γ_{sv}, and γ_{lv} denote the surface tension of the solid–liquid, solid–vapor, and liquid–vapor interfaces, respectively.[44] Since Young's equation presumes an ideal system with a perfectly flat and homogeneous surface, for the rough and structured surface, Wenzel proposed a fully wetting model, while Cassie and Baxter put forward a non-wetting model based on Young's equation. Figures 1a and 1b show schematics of the wetting states described by Wenzel and Cassie–Baxter.

In the Wenzel model, the contact angle θ_W is

$$\cos\theta_W = r_w \cos\theta_Y \quad (2)$$

where r_w is the area ratio of the structured surface to the corresponding flat surface.[19] In the Cassie–Baxter model, the contact angle θ_C is,[20]

$$\cos\theta_C = \Phi\cos\theta_Y + (1-\Phi)\cos 180° \quad (3)$$

where solid fraction Φ is the ratio of solid area to the apparent area at thashe structured surface.

However, the validity of these classical descriptions remains questionable in nano/microscale system applications for real, rough surfaces, and the explanation for the existing static intermediate state is insufficient. To obtain a better understanding on the static intermediate state, we proposed a partial wetting model, initially based on molecular dynamics simulations method.[28] As shown in Fig. 1c, the proposed model describes the degree of wetting in the concave volume of surface structures by applying liquid wetting ratio and contact angle as follows,

$$\cos\theta = \Phi_{sl}\cos\theta_Y + \Phi_{lv}\cos 180° \quad (4)$$

where Φ_{sl} and Φ_{lv} are the area ratio of the solid–liquid and liquid–vapor interface to the flat surface, respectively.

2.2 Theoretical Derivation of Partial Wetting Model Based on thermodynamic analysis.

Suppose a droplet is placed on a perfectly flat solid surface with a constant contact angle θ, under the assumption of zero gravity and ideal thermal equilibrium in the system. For a flat surface of total area A, the areas of the liquid–

vapor interface A_{lv}, the solid–liquid interface A_{sl} and the solid–vapor interface A_{sv} are

$$A_{lv} = 2\pi R^2 (1-\cos\theta)$$

$$A_{sl} = \pi (R\sin\theta)^2$$

$$A_{sv} = A - A_{sl} \tag{5}$$

where R is the contact radius of the droplet. The total surface energy of the system E is

$$E = A_{sl}\gamma_{sl} + A_{sv}\gamma_{sv} + A_{lv}\gamma_{lv} \tag{6}$$

Similarly, for a droplet at the structured surface, the total energy of the system E' is,

$$E' = A_{sl}'\gamma_{sl} + A_{sv}'\gamma_{sv} + A_{lv}'\gamma_{lv} \tag{7}$$

where A_{sl}', A_{sv}', A_{lv}' are the areas of solid–liquid interface, solid–vapor interface, and liquid–vapor interface respectively, depending on the wetting state. The area of A_{sl}', has a maximum value of $A_{sl}\times r_w$ for the fully wetting state of the Wenzel model, while has a minimum value of $A_{sl}\times\Phi$ for the non-wetting state of Cassie–Baxter model. For the intermediate state of the partial wetting model, the area of A_{sl}' is larger than $A_{sl}\times\Phi$ but smaller than $A_{sl}\times r_w$ and can be written as

$$A_{sl}' = A_{sl}\left[\Phi + (r_w - \Phi) f\right] \tag{8}$$

where f is defined as the effective wetting ratio inside the structures, associating with the increment of the wetted area at the structured surface. Accordingly, A_{sv}', A_{lv}' can be written as

$$A_{sv}' = Ar_w - A_{sl}\left[\Phi + (r_w - \Phi) f\right]$$

$$A_{lv}' = A_{lv} + A_{sl}(1-\Phi)(1-f) \tag{9}$$

and the total energy of the system shown in Eq. (7) becomes

$$\begin{aligned} E' = {} & A_{sl}\left[\Phi + (r_w - \Phi) f\right](\gamma_{sl} - \gamma_{sv}) \\ & + [A_{lv} + A_{sl}(1-\Phi)(1-f)]\gamma_{lv} + Ar_w\gamma_{sv} \end{aligned} \tag{10}$$

Substituting Eq. (5) to Eq. (10), the total differential of Eq. (10) results in

$$\begin{aligned} dE' = {} & \left[2\pi R\sin^2\theta dR + 2\pi R^2\sin\theta\cos\theta d\theta\right]\left[\Phi + (r_w - \Phi) f\right](\gamma_{sl} - \gamma_{sv}) \\ & + \left[4\pi R(1-\cos\theta)dR + 2\pi R^2\sin\theta d\theta\right]\gamma_{lv} \\ & + \left[\left(2\pi R\sin^2\theta dR + 2\pi R^2\sin\theta\cos\theta d\theta\right)(1-\Phi)(1-f)\right]\gamma_{lv} \end{aligned} \tag{11}$$

Since the variation of energy should be satisfied to $dE' = 0$ based on the energy minimization for the equilibrium system, thus, we can obtain

$$\left[\Phi + (r_w - \Phi) f\right](\gamma_{sv} - \gamma_{sl}) - \left[\cos\theta + (1-\Phi)(1-f)\right]\gamma_{lv} = 0 \tag{12}$$

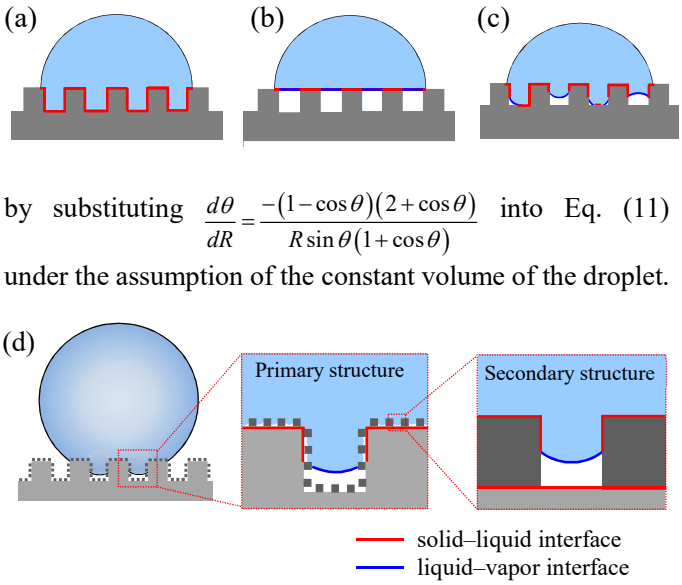

Fig. 2 Schematics of the wetting models on structured surfaces: (a) Wenzel model, (b) Cassie–Baxter model, (c) partial wetting model for one-scale structured surface and (d) partial wetting model for dual-scale structured surface. The red and blue lines indicate the ratio of the

by substituting $\frac{d\theta}{dR} = \frac{-(1-\cos\theta)(2+\cos\theta)}{R\sin\theta(1+\cos\theta)}$ into Eq. (11) under the assumption of the constant volume of the droplet. Therefore, the contact angle becomes

$$\cos\theta = \left[\Phi + (r_w - \Phi) f\right]\cos\theta_Y + (1-\Phi)(1-f)\cos 180° \tag{13}$$

Defining $\Phi_{sl} = \Phi + (r_w - \Phi) f$ and $\Phi_{lv} = (1-\Phi)(1-f)$, the contact angle for the partial wetting model shown in Eq. (4) can be derived.

As shown in Fig. 2, Φ_{sl} results in the surface area increment ratio r_w ($=A_{sl}/A = \Phi+(r_w-\Phi)\times 1$) for the Wenzel state; the solid fraction Φ ($=A_{sl}/A=\Phi+(r_w-\Phi)\times 0$) for the Cassie–Baxter state. Also, Φ_{lv} results in 0 for the Wenzel state, while results in $1-\Phi$ for the Cassie–Baxter state. That is, for the intermediate state of partial wetting, $\Phi < \Phi_{sl} < r_w$, while $0 < \Phi_{lv} < 1-\Phi$.

Φ_{sl} and Φ_{lv} are proposed for a general wetting state which might be a uniform intermediate wetting state or a mixed intermediate wetting state[45] as shown in Fig. 2c. For a surface of given structural parameters of Φ and r_w, the theoretical contact angle can be described by Eq. (4). However, the effective wetting ratio f is an unknown factor. An empirical method to determine f will be discussed in a later section.

The intermediate state of partial wetting at nano/micro hierarchically structured surfaces is shown in Fig. 2d. The ratio of the solid–liquid interface area to the apparent contact area for the hierarchical structured surface becomes to $\Phi_{sl1}\times\Phi_{sl2}$ and that of the liquid–vapor interface area to the apparent contact area becomes to $\Phi_{lv1}+\Phi_{sl1}\times\Phi_{lv2}$. Here, the Φ_{sl1}, Φ_{lv1} are the area ratios of the solid–liquid and liquid–vapor interface to the flat surface at the primary structure and Φ_{sl2}, Φ_{lv2} are those at the secondary structure.

Considering the similarity of the wetting state between the primary structures and the secondary structures, where $\Phi_{sl1}=\Phi_{sl2}=\Phi_{sl}$ and $\Phi_{lv1}=\Phi_{lv2}=\Phi_{lv}$, the ratio of the solid–liquid interface area to the apparent contact area for the hierarchical structured surface becomes to $\Phi_{sl}\times\Phi_{sl}$, and that of the liquid–vapor interface area to the apparent contact area is $\Phi_{lv}+\Phi_{sl}\times\Phi_{lv}$. Therefore, the contact angle of a nano/micro hierarchically structured surface can be used in the following equation.

$$\cos\theta_2 = \Phi_{sl}^2\cos\theta_Y + \left(\Phi_{lv}+\Phi_{sl}\Phi_{lv}\right)\cos 180° \qquad (14)$$

2.3 Experimental methods

Anodization (photo-assisted electrochemical etching) and chemical etching methods were used to prepare surfaces with micro- and nano/micro hierarchical structures. We prepared 83 Si samples including 42 porous surfaces, 29 patterned surfaces and 12 hierarchical nano/microstructured surfaces. All of the substrates have same chemical composition but different physical morphology.

Porous Si surfaces. To fabricate porous surfaces, n-type (100) Si substrates of 2 cm × 2 cm were anodized in a hydrofluoric acid electrolyte solution at the etching area of 0.636 cm^2.[11] The photo-assisted anodized process is under a metal halide light source (MME-250, MORITEX, Japan). The detailed anodic etching conditions are listed in Table 1. The pores of 1–6 μm in diameter were obtained at the anodic etching area. The pores grew to 80–120 μm in length through the cross-section of the Si wafer proportional to the etching time. The SEM images shown in Fig. 3 are the typical top view of the porous Si surfaces after the anodization process. We can find pores covered the surface randomly and the mean pore diameter d is ~2–3 μm. Since the total pore area A_{pore} in the given area A of the surface image can be obtained by integrating the area of each pore based on the surface image analysis (Fig. 3c), the solid fraction Φ of porous surface is determined by $1-A_{pore}/A$, ranging from 0.13 to 0.91 for the fabricated samples (Figs. s2-s4 in supplementary information). Fig. 4a shows the typical inclined view image of the porous Si surface. The side surface is covered with nano needle-like structures and micropores, while the surfaces inside of the micropores show a close similarity to the top surface.

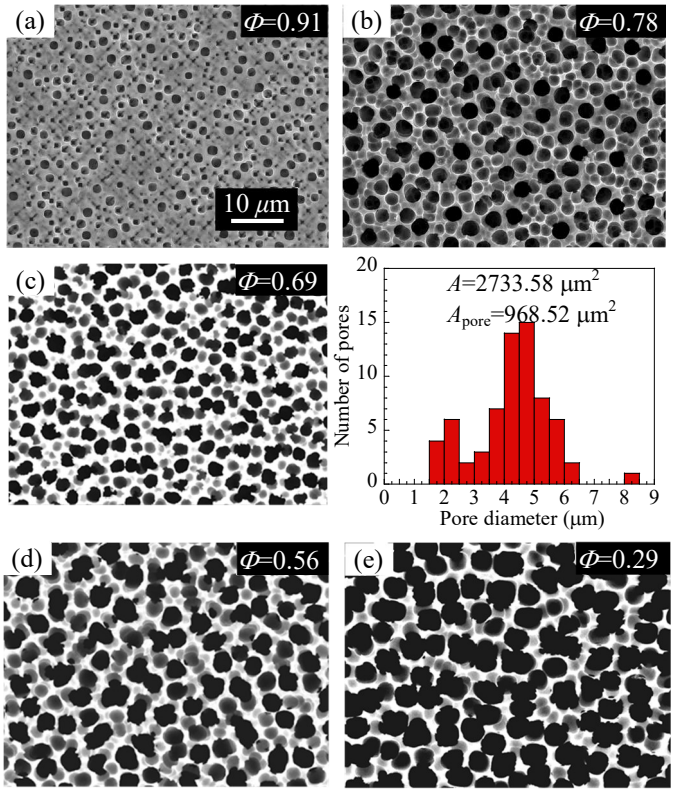

Fig. 3 Typical top views of porous Si surfaces: (a) Φ=0.91, (b) Φ=0.78, (c) Φ=0.69 with its histogram of pore diameter distribution, (d) Φ=0.56 and (e) Φ=0.29.

Table 1. Parameters of anodic etching to fabricate structured Si surfaces.[11,12]

Samples	Porous Si	Hierarchical Si
Irradiation intensity [Lx]	180000–270000	180000–270000
Electrolyte solution concentration [%]	4–23	15
Voltage [V]	2–30	5
Current density [mA/cm^2]	5–150	30–50
Etching time [min]	60–240	60–120

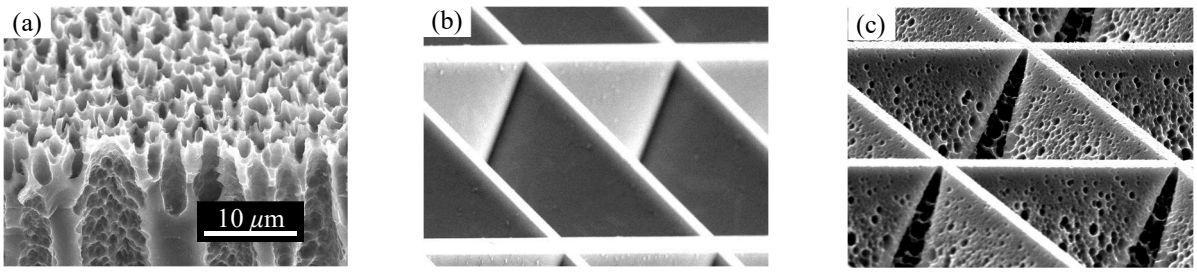

Fig. 4 Typical inclined views of structured Si surfaces: (a) porous Si, (b) patterned Si and (c) nano/micro hierarchical structured Si.

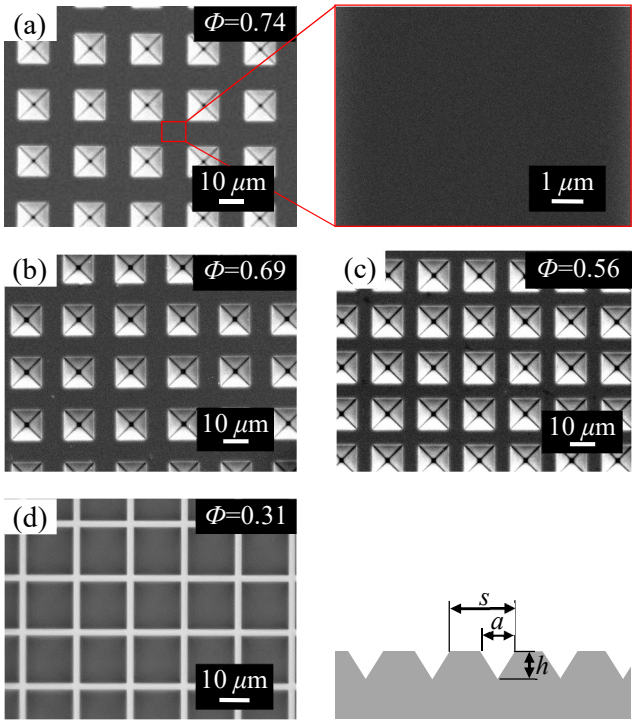

Fig. 5 Typical top views of patterned Si surfaces: (a) Φ=0.74, (b) Φ=0.69, (c) Φ=0.56 and (d) Φ=0.31.

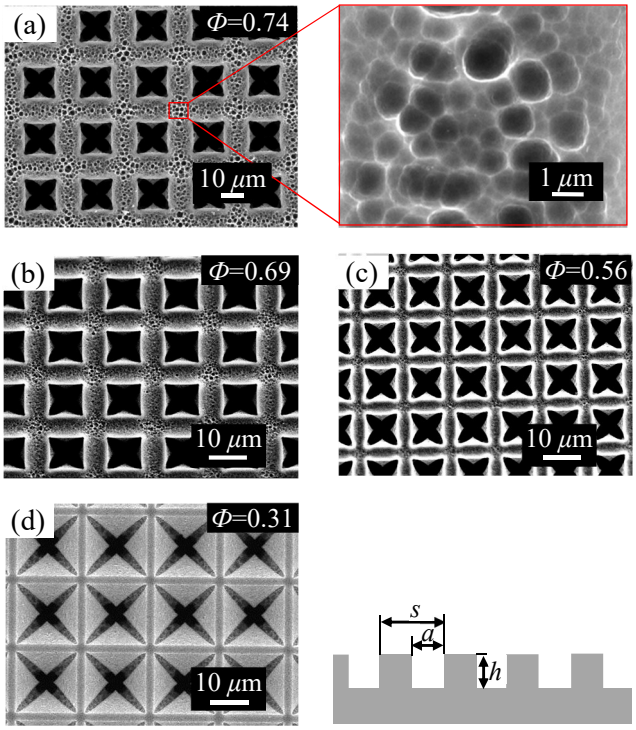

Fig. 6 Typical top views of nano/micro hierarchically structured Si surfaces: (a) Φ=0.74, (b) Φ=0.69, (c) Φ=0.56 and (d) Φ=0.31.

Patterned Si surfaces. The conventional wet chemical etching used in microfabrication was employed to prepare the patterned microstructured surfaces. Anisotropic wet-etched surfaces were prepared at the n-type (100) Si substrate of 2 cm × 2 cm, resulting to uniform micropores in an area of ~1 cm^2. The square orifices of the pores were a, ranging from 5 to 140 μm and the pitches separating the pores were $s - a$, ranging from 3 to 12 μm. Hence, the surface solid fraction could be estimated as $(s^2 - a^2)/s^2$. SEM images shown in Fig. 5 are the typical top views of the patterned Si surfaces. Since the depth of the pores, h, was limited to 13 μm, the pore arrays were in triangular, trapezoidal cross-sections (with a specific angle of 54.74 degree between the (111) and (100) planes due to anisotropic wet-etching on (100) Si) as shown in the schematic side views.

Hierarchical structured Si surfaces. A combination of microelectromechanical fabrication technology and photo-assisted anodic etching methods were employed to fabricate the hierarchical structured surfaces.[12] Further anodic etching of the patterned Si surface was performed under the conditions shown in Table 1. As shown in Figs. 4b and 5, the patterned Si surfaces are almost flat before anodic etching. Compared with the patterned Si surfaces, smaller and denser nanoscale needle-like structures are generated on the top of the patterned surface and inside the pores after anodic etching as shown in Figs. 4c and 6. That is, the anodic etched patterned Si surfaces have structures over the range of length from nanoscale to microscale, and formed nano/micro hierarchical structured surfaces.

2.4 Surface Characterization

Fractal dimension analysis on surface images were carried out with the aid of fractal analysis software (fractal3, Ver. 3.4.7, NARO). The fractal dimension D is obtained from the gray scale images by box counting method. For porous Si, D was ~2.4, while that for the patterned microstructured Si was ~2.2 (see Figs. s5 and s6 in supplementary information).

To isolate the effect of physical morphology on surface wettability, all of the substrates were prepared carefully to have same chemical composition but different physical morphology. Both acetone and buffered hydrofluoric acid solutions were used to remove contamination and silicon oxide film from the Si surfaces in the ultrasonic bath, and then rinsed by pure water repeatedly. The water contact angle (WCA) was measured with a microscope system (Keyence VH-200) using $\theta/2$ method at 25 °C.[46,47] Pure water (Kishida Chemical, electrical resistivity 18 MΩ·cm) was supplied to the surfaces using a micro-syringe with a constant volume of 4 μL. Before WCAs measurement at the etched area, the WCA at the un-etched area for every sample has been confirmed to be the same as that at the flat surface

of θ_Y (79.5°±1.5°). That is, all of the samples almost have same chemical compositions. To prevent the contamination and evaporation at the droplet surface, the measurement of WCA has been carried out within 10 minutes after surface cleaning, covered with a measurement cell (see Fig. s8 in supplementary information). Each static WCA test was repeated five times, and the results were averaged for use in subsequent analysis.

3 Results and discussion

3.1 Water contact angles (WCAs)

Figure 7 shows the WCAs on the micro- and hierarchically structured Si surfaces as a function of solid fraction Φ. The WCA on flat surface (Φ=0 or 1) is 79.50° and those on the porous Si surfaces are varied from 91.50° to 129.57° (Φ=0.13~0.91), having the maximum WCA of θ_{max}=129.57° at Φ=0.49 as shown in Fig. 7a. The WCAs increase with increasing solid fraction in the range of Φ<0.49, while decreased in the range of Φ>0.49. It is clear that the geometrical nano/microstructures of porous Si can improve surface hydrophobic properties. Also, the results indicate that the solid fraction is a dominant physical factor affecting the surface wettability.

Experimental WCA results on patterned Si and hierarchically structured Si surfaces are presented in Fig. 7b. The WCAs on patterned Si surfaces (blue squares) increase as increasing solid fraction before reaching a maximum value of 125.96° at Φ=0.11 and then decrease gradually. The patterned Si surfaces with primary microscale structures display hydrophobicity and the WCAs are much larger than those measured at the flat Si (un-etched area). Furthermore, the hierarchical structured Si surfaces with nanoscale needle-like structures show enhanced hydrophobicity and the WCAs (red squares) are larger than those of patterned Si surface with the maximum WCA of 146.60° obtained at Φ=0.38.

3.2 Effective wetting ratio

Effective wetting ratio f is defined as the proportion of solid–liquid contact area to the apparent area inside of the structures, ranging between 0 (Cassie–Baxter state) and 1 (Wenzel state). Since it is an unknown factor, we obtain the effective wetting ratio based on Eqs. (4) and (14) by substituting the experimental WCAs θ, θ_Y and the structured parameters Φ and r_w. As described in Section 2.3, for the patterned and hierarchical structured Si surfaces, Φ can be determined directly by the structure parameters a and s; while it is obtained by the image analysis of surface morphology for the porous Si surface. The method to obtain r_w is a little complex. On the one hand, r_w can be calculated using a, s, h and the specific angle (54.7° with respect to the (100) Si wafer surface) according to its triangular

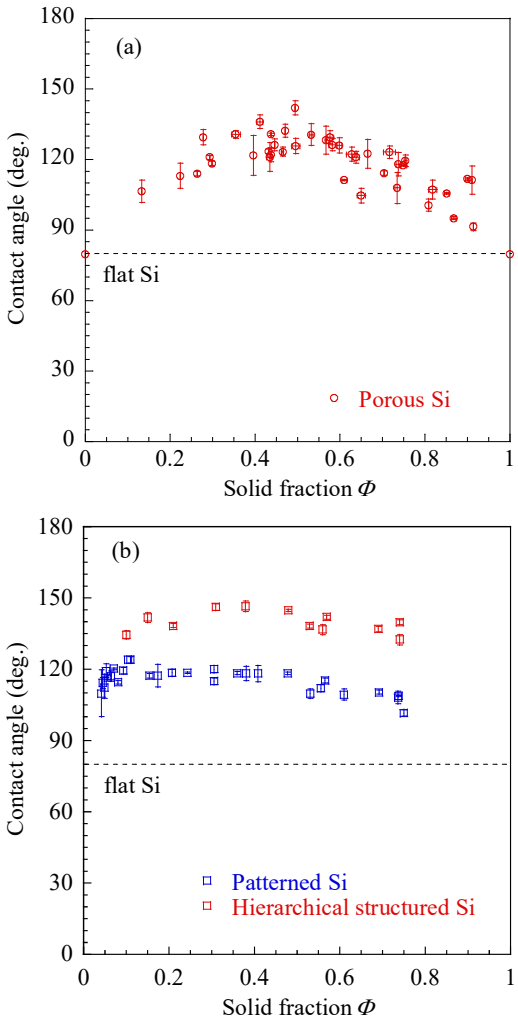

Fig. 7 Experimental WCA results of (a) porous Si and (b) patterned Si and hierarchically structured Si.

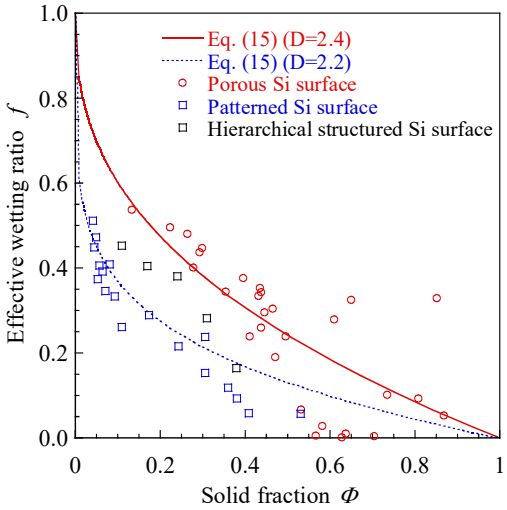

Fig. 8 Effective wetting ratio as a function of solid fraction s and fractal dimension D.

/trapezoidal cross-section for the patterned Si surface. On the other hand, for the porous and hierarchical structured Si surfaces, r_w is estimated using the side area of pores $l_p \times h_e$, where l_p is the perimeter of pore orifice ($l_{p\text{-porous}}=\pi d$, $l_{p\text{-hierarchical}}=4a$) and h_e is the equivalent height of the pores. Although r_w results in extremely large value up to more than 100 for the high aspect ratio pores generated at the porous Si or hierarchical Si substrates, the maximum equivalent $r_{w\text{-max}}$ is up to the Wenzel model's limit of 5.49 for $\theta_Y=79.50$ ($r_{w\text{-max}}=1/\cos\theta_Y$). That is, the effect of the pore height on the effective wetting ratio is limited to an equivalent height, where the equivalent height is estimated at $r_{w\text{-max}}$.

As shown in Fig. 8, the estimated effective wetting ratio f decreased with increasing solid fraction Φ and also showing a dependence on the fractal dimension D. The fitted curves as a function of the solid fraction and the fractal dimension showing in Eq. (15), has been proposed empirically.

$$f = 1 - \Phi^{D-2} \quad (15)$$

Although some data scattering exists, Eq. (15) roughly agree with the data estimated from the experiments as shown in Fig. 8. Hence, we use Eq. (15) to indicate the effective wetting ratio f for the calculation of partial wetting model shown in Eqs. (4)-(14).

3.3 Comparisons between experimental and theoretical results

Comparisons between the experimental WCAs at the structured Si surfaces and the theoretical wetting models are given in Fig. 9. The experimental WCAs of the structured Si surfaces (circles and squares) shows a deviation from either Wenzel (dash line) or Cassie–Baxter (dot line) models. We also plotted the theoretical predictions based on Eqs. (4) and (14) of the partial wetting model. As shown in Fig. 9a, the predicted data of Eq. (14) (red line) are consistent with the experimental WCAs of porous Si surfaces. This implies that the contact mode at the porous surface differs from the classical fully wetting or non-wetting models. That is, an intermediate state between the Wenzel and Cassie–Baxter states exists at the porous Si surfaces. Similar results were obtained for patterned and hierarchically structured Si surfaces (Fig. 9b), where the blue and red curves indicate the theoretical partial wetting model of one-scale and dual-scale structured surface. The WCAs at patterned Si surfaces (blue open squares) agree fairly well with the Eq. (4). On the other hand, the WCAs at the hierarchical structured Si surfaces (red open squares) deviate slightly from Eq. (14) but show better agreement than the classical Wenzel and Cassie–Baxter models.

The theoretical model of the partial wetting proposed in this study agrees with the experimental results in general. However, there are still few limitations. One is the difficulty to estimate the solid fraction and the surface area increment ratio on the dual-scale structures. To simplify the theoretical prediction for the hierarchical structured surfaces, we made an assumption about the similarity of the wetting state between the primary structures and the secondary structures.

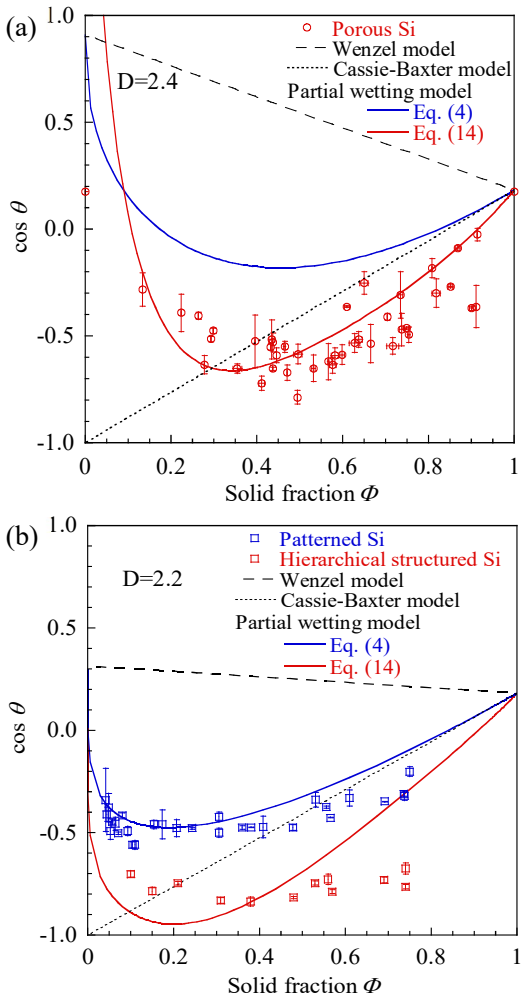

Fig. 9 Comparisons of experimental results and theoretical models for (a) porous surfaces and (b) patterned and nano/micro hierarchically structured surfaces.

Eq. (14) is based on this assumption. Another limitation is the difficulty to estimate the equivalent height of the high-aspect-ratio pore for the porous Si and hierarchical Si substrates. We employed an approximation of the equivalent height from the maximum equivalent $r_{w\text{-max}}$ ($r_{w\text{-max}}=1/\cos\theta_Y$) of Wenzel model. However, these assumption and approximation need verification. Further investigation on the accurate estimation of the effective wetting ratio is required.

4 Conclusions

We derived the theoretical partial wetting model for the static intermediate wetting state based on the thermodynamic energy minimization method. Our experimental results show good agreement with the proposed partial wetting model but deviate significantly from the classical Wenzel and Cassie–Baxter models. We conclude that the proposed partial wetting model takes advantage of describing the static intermediate wetting state between fully wetting and non-wetting states for a general solid–liquid contact mode.

Since disagreements between the previous experimental results and classical theoretical models existed, our partial wetting model is expected to address previous unclear issues on wetting. We have confirmed the dependence of surface wettability on the physical morphology at both micro- and nano/micro hierarchically structured Si surfaces, where the solid fraction is one of the dominant factors to determine the intermediate wetting state. Since the solid fraction is a dimensionless factor, the critical size of the surface structure and the valid range of the partial wetting model are not addressed in this paper but should be worthy of future investigation.

Conflicts of interest

The authors declare no competing financial interest.

Acknowledgements

This work is partly supported by the Ministry of Education, Science and Culture of the Japanese Government through the Grant-in Aid for Scientific Research, Project No. 18H01385 and No. 21360099, the research foundation of Kyushu Institute of Technology, and the Initiative for Realizing Diversity in the Research Environment by Ministry of Education, Culture, Sports, Science and Technology, Japan. Ryuji Ando and Kazuya Mizumoto are acknowledged for their fabrication and measurement assistance. The micro-electro-mechanical fabrication used in this study was partly supported by the Kitakyushu Foundation for the Advancement of Industry, Science, and Technology.

References

1 S. Wang, K. Liu, X. Yao and L. Jiang, *Chem. Rev.*, 2015, **115**, 8230–8293.

2 H. Bellanger, T. Darmanin, E. Taffin de Givenchy and F. Guittard, *Chem. Rev.*, 2014, **114**, 2694–2716.

3 R. Raj, S. C. Maroo and E. N. Wang, *Nano Lett.*, 2013, **13**, 1509–1515.

4 T. S. Wong, S. H. Kang, S. K. Tang, E. J. Smythe, B. D. Hatton, A. Grinthal and J. Aizenberg, *Nature*, 2011, **477**, 443–447.

5 S. Shibuichi, T. Onda, N. Satoh and K. Tsujii, *J. Phys. Chem.*, 1996, **100**, 19512–19517.

6 H. Y. Wu and P. Cheng, *Int. J. Heat Mass Transfer*, 2003, **46**, 2547–2556.

7 B. R. Yang, W. Cao, G. S. Liu, H. J. Chen, Y. Y. Noh, T. Minari, H. C. Hsiao, C. Y. Lee, H. P. D. Shieh and C. Liu, *ACS Appl. Mater. Interfaces*, 2015, **7**, 21433–21441.

8 G. Nagayama and P. Cheng, *Int. J. Heat Mass Transfer*, 2004, **47**, 501–513.

9 E. Terrado, R. Molina, E. Natividad, M. Castro, P. Erra, D. Mishkinis, A. Torres and M. T. Martínez, *J. Phys. Chem. C*, 2011, **115**, 9312–9319.

10 A. Ressine, I. Corin, K. Jaras, G. Guanti, C. Simone, G. Marko-Varga and T. Laurell, *Electrophoresis*, 2007, **28**, 4407–4415.

11 G. Nagayama, N. Idera, T. Tsuruta, J. R. Yu, K. Takahashi and M. Hori, *Electrochemistry*, 2005, **73**, 939–941.

12 G. Nagayama, A. Kuromaru, M. Kaneda and T. Tsuruta, *Applied thermal engineering*, 2014, **72**, 298–303.

13 S. Herminghaus, *EPL (Europhysics Letters)*, 2000, **52**, 165–170.

14 Y. Kita, C. M. Dover, A. Askounis, Y. Takata and K. Sefiane, *Soft matter*, 2018, **14**, 9418–9424.

15 V. Zorba, L. Persano, D. Pisignano, A. Athanassiou, E. Stratakis, R. Cingolani, P. Tzanetakis and C. Fotakis, *Nanotechnology*, 2006, **17**, 3234–3238.

16 A. Askounis, D. Orejon, V. Koutsos, K. Sefiane, and M. E. Shanahan, *Soft matter*, 2011, **7**, 4152–4155.

17 Y. Yamada, T. Ikuta, T. Nishiyama, K. Takahashi and Y. Takata, *Langmuir*, 2014, **30**, 14532–14537.

18 H. C. Zhang, Y. Kita, D. J. Zhang, G. Nagayama, Y. Takata, K. Sefiane and A. Askounis, *Heat Transfer Eng.*, 2019, 1–9.

19 R. N. Wenzel, *Ind. Eng. Chem. Res.*, 1936, **28**, 988–994.

20 A. B. D. Cassie and S. Baxter, *Trans. Faraday Soc.*, 1944, **40**, 546–551.

21 E. Bormashenko, *Adv. Colloid Interface Sci.*, 2015, **222**, 92–103.

22 M. Miwa, A. Nakajima, A. Fujishima, K. Hashimoto and T. Watanabe, *Langmuir*, 2000, **16**, 5754−5760.

23 A. Marmur, *Langmuir*, 2003, **19**, 8343–8348.

24 C. Luo, M. M. Xiang and X. Heng, *Langmuir*, 2012, **28**, 9554−9561.

25 C. Luo and M. M. Xiang, *Microfluidics and Nanofluidics*, 2014, **17**, 539−548.
26 J. Yang, J. Wang, C. W. Wang, X. He, Y. Li, J. B. Chen and F. Zhou, *Thin Solid Films*, 2014, **562**, 353–360.
27 D. Lei, Y. Li, M. Lin and M. Wen, *J. Phys. Chem. C*, 2019, **123**, 18376–18386.
28 G. Nagayama, S. Shi-iki and T. Tsuruta, *Trans Japan Soc. Mech. Eng. B*, 2007, **73**, 1084–1091.
29 T. Koishi, K. Yasuoka, S. Fujikawa, T. Ebisuzaki and X. C. Zeng, *Proc. Natl. Acad. Sci.*, 2009, **106**, 8435–8440.
30 A. Lafuma and D. Quéré, *Nat. Mater.*, 2003, **2**, 457–460.
31 N. A. Patankar, *Langmuir*, 2004, **20**, 7097–7102.
32 G. McHale, S. Aqil, N. J. Shirtcliffe, M. I. Newton, and H. Y. Erbil, *Langmuir*, 2005, **21**, 11053–11060.
33 P. Papadopoulos, L. Mammen, X. Deng, D. Vollmer and H. J. Butt, *Proc. Natl. Acad. Sci.,* 2013, **110**, 3254–3258.
34 B. He, N. A. Patankar and J. Lee, *Langmuir*, 2003, **19**, 4999–5003.
35 G. Wang, Z. H. Jia and H. N. Yang, *Colloid Polym. Sci.*, 2016, **294**, 851–858.
36 Y. Liu and C. H. Choi, *Colloid. Polym. Sci.*, 2013, **291**, 437–445.
37 H. Y. Erbil, and C. E. Cansoy, *Langmuir*, 2009, **25**, 14135–14145.
38 C. E. Cansoy, H. Y. Erbil, O. Akar and T. Akin, *Colloids Surf. A*, 2011, **386**, 116–124.
39 J. H. Poynting and J. J. Thomson, *Properties of Matter*, eighth ed., Griffin, London, 1902, 139–140.
40 P. Roura and J. Fort, *J. Colloid Interface Sci.*, 2004, **272**, 420–429.
41 G. McHale, *Langmuir*, 2007, **23**, 8200–8205.
42 S. H. Sajadinia and F. Sharif, *J. Colloid Interface Sci.*, 2010, **344**, 575–583.
43 H. P. Wu, K. Zhu, B. B. Wu, J. Lou, Z. Zhang and G. Z. Chai, *Appl. Surf. Sci.*, 2016, **382**, 111–120.
44 T. Young, *Phil. Trans. Roy. Soc.*, 1805, **95**, 65–87.
45 S. Kojevnikova and A. Marmur, *Colloids Surf. A*, 2017, **521**, 78–85.
46 M. W., Yang and S. Y., Lin, *Colloids Surf. A* 2003, **220**, 199–210.
47 A. F., Stalder, T., Melchior, M., Müller, D., Sage, T., Blu and M. Unser, *Colloids Surf. A* 2010, **364**, 72–81.